

Journal of Materials Chemistry A

Accepted Manuscript



This is an *Accepted Manuscript*, which has been through the Royal Society of Chemistry peer review process and has been accepted for publication.

Accepted Manuscripts are published online shortly after acceptance, before technical editing, formatting and proof reading. Using this free service, authors can make their results available to the community, in citable form, before we publish the edited article. We will replace this *Accepted Manuscript* with the edited and formatted *Advance Article* as soon as it is available.

You can find more information about *Accepted Manuscripts* in the [Information for Authors](#).

Please note that technical editing may introduce minor changes to the text and/or graphics, which may alter content. The journal's standard [Terms & Conditions](#) and the [Ethical guidelines](#) still apply. In no event shall the Royal Society of Chemistry be held responsible for any errors or omissions in this *Accepted Manuscript* or any consequences arising from the use of any information it contains.



ARTICLE

Received 00th January 20xx,
Accepted 00th January 20xx

DOI: 10.1039/x0xx00000x

www.rsc.org/

Enhanced Hydrogen and Methane Storage of Hybrid Mesoporous Organosilicas

Georgios N. Kalantzopoulos,^{*a} Myrsini K. Antoniou,^a Apostolos Enotiadis,^b Konstantinos Dimos,^b Enrico Maccallini,^a Alfonso Policicchio,^a Elio Colavita^a and Raffaele G. Agostino^a

In this study hybrid Mesoporous Organosilicas (HMOs) were synthesized by using tetra-ethyl-orthosilicate (TEOS) as silica source and 1,4-bis(tri-ethoxysilyl)benzene (BTB) in various BTB/TEOS ratios. The two extreme cases of 0 and 100 mol% BTB are compared with partial addition of BTB (25 mol%) and partial absence of TEOS (75 mol% BTB). The synthesized mesoporous materials are characterized by means of Powder X-ray Diffraction (PXD), Scanning Electron Microscopy (SEM) and helium pycnometry for the skeletal density evaluation. The Brunauer-Emmett-Teller (BET) method is used for the determination of the specific surface area (SSA) and Non-local Density Function Theory (NLDFT) calculations are applied for the evaluation of their Pore Size Distribution (PSD). Their hydrogen and methane sorption properties are investigated with a Sieverts apparatus under isothermal sorption equilibrium conditions at cryogenic and close to ambient temperatures, respectively. In hydrogen the combination of phenyl rings along with pores in the micro-/mesoporous border resulted in increased sorption capacity. The simultaneous presence of two different precursors increased the surface inhomogeneity leading to a wider distribution of adsorption sites close to the micro-/mesopore border regime that favored the hydrogen sorption properties. The presence of the phenyl rings doubled the number of methane molecules the material surface can accommodate. Partial substitution of TEOS by BTB (25 mol%) gave the same adsorbed methane density as the non-hybrid material consisted of 100% BTB. The materials exhibited excellent reversibility and sorption stability over aging. Their sorption performance was evaluated with the Tóth model and was correlated with their structural characteristics. The fraction of micropores over the total pores was quantitatively correlated with the maximum storage capacity and the adsorbant-adsorbent interaction strength. Finally, in methane and for low coverage the enthalpy of adsorption was calculated with the Clausius–Clapeyron equation.

^a CNISM-Department of Physics, Univ. of Calabria, via P. Bucci 33C, 87036, Rende (CS), Italy.

^b Department of Materials Science & Engineering, University of Ioannina, 45100 Ioannina, Greece.

† Footnotes relating to the title and/or authors should appear here. Electronic Supplementary Information (ESI) available: [details of any supplementary information available should be included here]. See DOI: 10.1039/x0xx00000x

Introduction

During the recent years significant research has been taking place in substituting carbon-based energy tapping to alternative, pollutant-free methods that are going to decrease the CO₂ emissions responsible for the climate change.^{1,2} In this aspect hydrogen (H₂) contains 3 times higher energy density per mass compared to gasoline. At the same time methane (CH₄), that is the main component of natural gas, has lower carbon footprint than the higher carbon-containing petroleum derivatives and can be used as an intermediate step in the fossil-to-hydrogen transition period. The pursue of a material that can host in ambient conditions and relatively low pressures the amount of hydrogen necessary enough to power an automobile autonomously for 500 km² has been the goal for numerous research Institutes and industry around the globe. In this aspect both the U.S. Department of Energy (DoE) and the European Union Fuel Cells and Hydrogen Joint Technology Undertaking (FC-HJU) have issued recommendations on the performance targets required for materials, fuel cell technology and the complete gas storage tank system.^{3,4}

Considerable amount of research has been carried out on chemical and physical storage of hydrogen up to date. Chemical storage of hydrogen involves its dissociation and creation of a hydride through a single- or multiple- phase transformation in the metals bulk.^{5, 6} Hydrides with high storage capacity require substantial amount of energy in order to release hydrogen back.⁷ When decrease in the desorption temperature is achieved, the desorption kinetics are usually decreased and the re-absorption is rather slow due to kinetic barriers that the rehydrogenation of amorphous phases employs.⁸ On the other hand, hydrides that require small amount of energy for hydrogen release do not exhibit significant sorption capacities.⁹ Moreover the hydrogen absorption mechanism that governs this type of materials involves slow kinetics,⁶ due to the multiple phase transformations involved. These issues can be resolved with hydrogen physisorption onto porous materials. During the last years different families of porous solids such as the zeolites, metal-organic frameworks (MOFs) and covalent organic frameworks (COFs) have been studied as potential hydrogen¹⁰ or methane adsorbents¹¹.

The zeolites possess well-ordered crystalline structure and tunable pore size but their relatively restricted specific surface area (SSA, typically less than 1000 m²g⁻¹)¹² restrains them from adsorbing sufficient amounts of hydrogen.¹³ MOFs have been extensively studied as hydrogen storage materials with their adsorption capacity to be attributed to their large SSA.^{10, 14} As a pathway to enhance the surface-to-molecule interaction, partial functionalization has been applied by doping the MOFs surface with Li⁺ atoms, with promising results.^{15, 16} However, rather limited amount of experimental work on their sorption properties has been done up to date, mainly due to their structural instability in non-ambient pressures.^{17, 18}

The key for enhancing the storage capacity in porous materials is through reinforcing the interaction between the hydrogen and the adsorbent's surface. Proper selection of the building units and enrichment of the adsorbent's surface with atoms that attract hydrogen molecules can strongly enhance the hydrogen molecule – surface interaction.¹⁹ The effect of surface functionalization and variation of the building constituents on the adsorption properties has not been thoroughly examined up to now. A material family that allows this study is the Periodic Nano-/Mesoporous Organosilicas (PMOs).²⁰⁻²³

Due to their functionalization, PMOs permit the study and comprehension of each synthesis parameter effect on the sorption properties, an ability that had not been examined in that degree till today. Recently, PMO were synthesized under basic conditions and their structural and hydrogen sorption properties were investigated. That study demonstrated that the adsorbent's amorphous structure and the use of shorter surfactant in the synthesis enhance both storage capacity and strength of interaction between the surface and the adsorbate.²⁴ Similarly, naphthalene-based PMOs we synthesized²⁵ and their hydrogen and methane sorption properties were investigated²⁶ and revealed enhanced sorption capacity compared to MCM-41.

In this paper, hybrid PMOs are synthesized by using tetraethyl-orthosilicate (TEOS) as silica source and 1,4-bis(triethoxysilyl)benzene (BTB) in various BTB ratios. The two extreme cases of 0 and 100 mol% BTB are compared with partial addition of BTB (25 mol% BTB) and partial absence of TEOS (75 mol% BTB). Their hydrogen and methane sorption properties are investigated with a Sieverts apparatus under sorption equilibrium conditions. The study aims to evaluate the effect that single- (non-hybrid Mesoporous Organosilicas) and double-precursors (HMOs) have on the sorption properties with hydrogen and methane. . The materials reversibility and sorption stability over time are also evaluated. Their sorption performance for both hydrogen and methane is evaluated using the Tóth model and correlated with their structural characteristics. Finally, in the case of methane and for low coverage the enthalpy of adsorption is evaluated with the Clausius–Clapeyron equation.

Experimental

Reagents

All materials were reagent or analytical grade and were used as purchased without further purification. Aqueous ammonia solution 25 wt% was purchased from Fluka (09860), cetyltrimethylammonium bromide (CTAB) 95% from Sigma-Aldrich (855820), tetraethylorthosilicate (TEOS) 98% from Sigma-Aldrich (131903), hydrochloric acid (HCl) 37 wt% from Merck (1.00317.2500), methanol 99.9+% from Merck (1.06009.1011), ethanol 99.5% from Panreac (121086.1212), and 1,4-bis(triethoxysilyl)benzene (BTB) 96% from Sigma-Aldrich (598038).

Synthesis

The hybrid periodic mesoporous materials were synthesized as follows: 20.53 g H₂O, 11.2 g of ammonium hydroxide solution (25 wt%), and 0.44 g CTAB were stirred for 30 min in a polypropylene bottle. 2.12 g TEOS were added drop wise and solution was stirred for another 30 min before ageing at 80 °C for 96 h. The white powder was collected by centrifugation, washed thoroughly with water, and air-dried under ambient conditions. In order to remove the surfactant, and thus to create open structures, the as-synthesized sample was stirred for 72 h in a refluxing solution of 20 g HCl (37 wt%) and 140 g of methanol. The corresponding periodic mesoporous silica (PMS) was collected by centrifugation, rinsed with methanol and ethanol, and air-dried under ambient conditions (sample: PMS). The hybrid PMOs samples were synthesized with the same protocol by substituting TEOS with BTB. 0.52 g BTB and 1.594 g TEOS were mixed for the preparation of sample PMO-25, and 1.576 g BTB and 0.534 g TEOS for sample PMO-75, while 2.097 g BTB and no TEOS were used for sample PMO-100.

Structural and Textural Characterization Techniques

X-ray powder diffraction (XRD) data were collected on a D8 Advance Bruker diffractometer using Cu K α (40 kV, 40 mA, $\lambda=1.54178$ Å) radiation and a secondary beam graphite monochromator. Diffraction patterns were collected in the 2 θ range from 2 to 80 degrees, in steps of 0.02 degrees and 2 s counting time per step.

Pellets of pulverized samples dispersed in KBr were used for recording Fourier transform Infrared spectra (FTIR) on a Perkin Elmer GX Fourier transform spectrometer in the frequency range of 400–4000 cm⁻¹. The reported spectra are an average of 64 scans at 2 cm⁻¹ resolution.

The nitrogen adsorption–desorption isotherms were measured at 77 K on a Sorptomatic 1990, thermo Finnigan porosimeter. Specific surface areas (SSA) were determined with the BET method in the range 0.05–0.25 by taking care that the pertinent consistency criteria are met^{27,28}. All samples used for the surface analysis were outgassed at 473 K for 20 h under high vacuum (10⁻⁵ mbar) before measurement. Non-local Density Function Theory (NLDFT) pore size distribution calculations were performed using the commercial software AS1Win from Quantachrome Instruments. The calculation method used, was N₂ at 77 K on silica, cylindrical pores, NLDFT adsorption branch or equilibrium kernel model.

Scanning electron images were recorded using a Quanta FEG 400 (FEI) scanning electron microscope (SEM). The SEM images were acquired by using an electron beam of 20 keV. The images provide the typical morphology of the samples powders deposited on carbon tape.

Hydrogen/Methane Sorption Assessment

The hydrogen and methane sorption measurements were carried out with an in-house made Sieverts' apparatus built by DeltaE S.r.l.²⁹ The volumetric gas storage apparatus consists of a gas manifold with a series of tubes and valves connecting the sample holder to the gas reservoirs void volume and pressure transducers.

Home-made algorithms built by Labview® calculate the adsorbed and desorbed gas molecules as well as the number of molecules per square nanometer adsorbed at any given pressure aliquot. The cryogenic measurements took place while keeping a fixed volume of the sample-holder in a liquid nitrogen bath. Typically 250 mg of each sample were inserted in the sample-holder. All samples were outgassed at 200 °C overnight prior to measurement.

Hydrogen (99.999% purity) sorption measurements took place in the pressure range 0 – 7 MPa at 77 K. Methane (99.995% purity) sorption measurements were carried out in the pressure range 0 – 4.5 MPa at 286, 298 and 313 K. He (99.999% purity) pycnometry measurements took place using He as the probe gas in room temperature and in the pressure range of (0 – 900) mbar. All pycnometry measurements were repeated at least 7 times to minimize the experimental error.

Results and Discussion

The XRD patterns of the samples with the different BTB content are shown in Fig. 1. As seen, the pattern of sample PMS is typical of materials classified in the *P6mm* space group with hexagonal arrangement of uniform pores displaying the characteristic strong (100) reflection at the low angle region, followed by the weak, although well resolved, (110) and (200) reflections. The substitution of TEOS with BTB causes progressive structure disordering moving from hexagonal *P6mm* to partly disordered – hexagonal structures. As the BTB percentage increases the (110) and (200) reflections become weaker and finally they are completely absent in the case of PMO-75 and PMO-100.²⁴ By applying Bragg's law for the first reflection peak, the d_{100} spacing is found to be 4.2, 4.0, 3.9 and 4.2 nm for the samples PMS, PMO-25, PMO-75 and PMO-100, respectively. The corresponding unit cell dimensions ($a_0=2d_{100}/\sqrt{3}$) are listed in Table 1.

The successful incorporation of BTB in the PMO samples is evident by their FTIR spectra (see Supporting Information Fig. S1). As observed, two peaks arise in the spectra with increasing BTB ratio, which are correlated with aromatic groups, verifying the presence of phenyl rings in the walls of the periodic mesoporous materials. The peaks at 3062 and 3013 cm⁻¹ are attributed to asymmetric and symmetric stretching vibrations of aromatic C-H bonds, respectively.²⁴

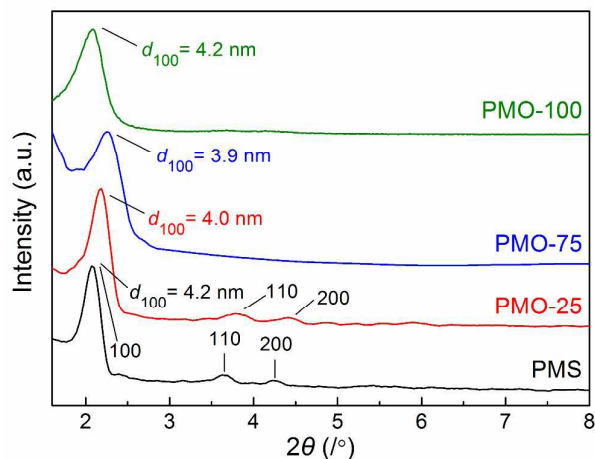


Fig 1 X-ray diffraction patterns of the as-synthesized samples.

The nitrogen adsorption-desorption isotherms of the samples and their corresponding NLDFT pore size distributions (PSD) are shown in Fig. 2. All the isotherms are classified as Type IV which is characteristic of mesoporous materials. The specific surface areas (SSA) were calculated using the BET equation and were found to be 953, 636, 1052, and 782 m²/g for samples PMS, PMO-25, PMO-75, and PMO-100, respectively.

Pore diameters from DFT calculations were found to be 4.1, 3.8, 3.5 and 3.5 nm in order of increasing BTB content, respectively. If we consider the low mesoporous regime, i.e. pore diameters below 2.7 nm, both hybrid materials (PMO-25 and PMO-75) have part of their pores in that region. On the other hand, both non-hybrid materials have narrow PSDs with PMO-100 having the narrowest PSD of all the samples which expands between 2.7 – 4.2 nm (Fig 2). Moreover, skeletal densities (measured by helium pycnometry) and pore volumes of the samples were evaluated and are listed in Table 1. The increase of the BTB ratio in the samples does not seem to give a trend either on the SSA or on the pore volume values. Although sample PMO-25 exhibits a high grade of ordering compared to samples with more BTB content, it displays the lowest values of SSA and pore volume. As expected, by increasing the BTB ratio, the skeletal density decreases significantly which is also a proof for the incorporation of the low-density phenyl rings in the walls of the porous materials. In addition, the pore diameter is slightly decreased from 4.1 to 3.5 nm, again with the increase of BTB ratio. On the contrary, when taking into account the estimated lattice parameters from XRD patterns, the samples have 0.8, 0.9, 1.0 and 1.4 nm wall thickness in increasing BTB content order, respectively.

Journal of Materials Chemistry A

ARTICLE

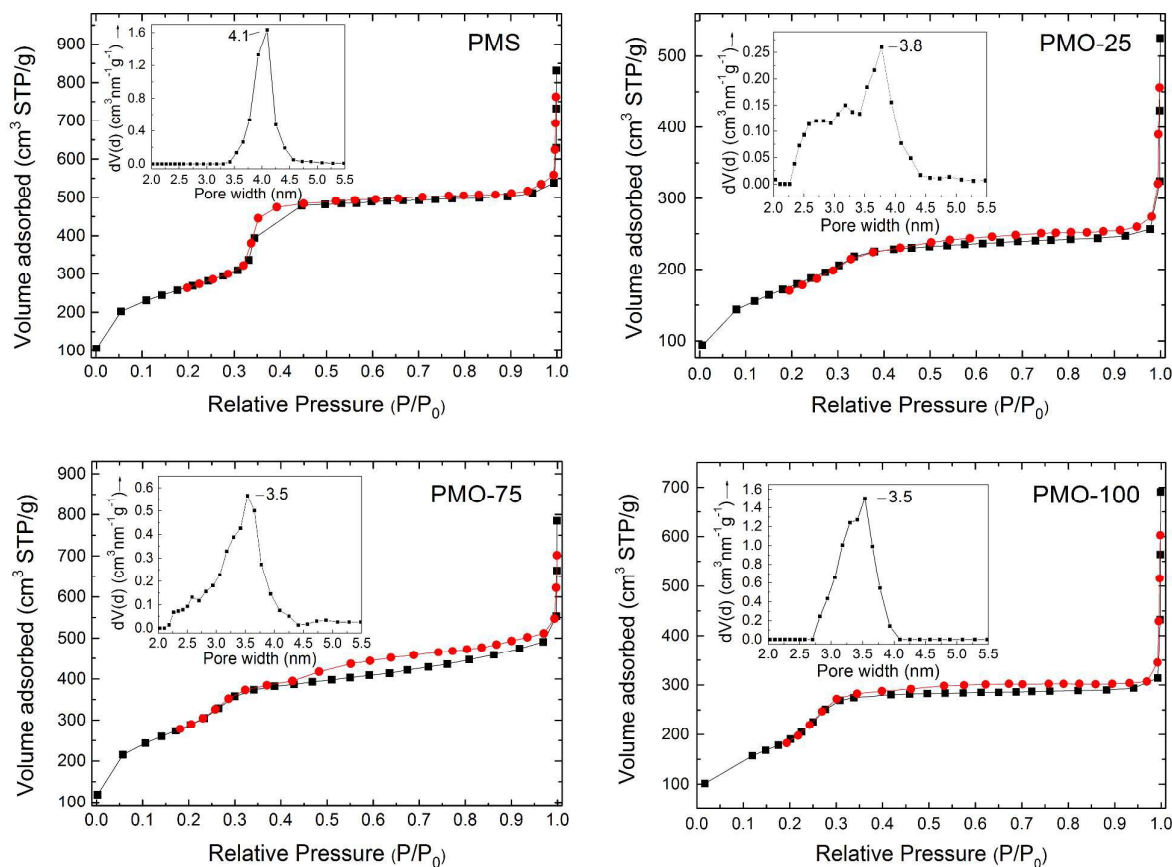


Fig 2 Nitrogen adsorption-desorption isotherms and the corresponding pore size distributions of the samples calculated using the Non-local Density Function Theory (insets).

Sample	Density (g/cm ³)	Specific surface area (m ² /g)	Pore diameter (nm)	Pore volume (cm ³ /g)	Crystallinity	Lattice parameter α_0 (nm)
PMS	2.8 ± 0.3	953	4.1	0.79	Ordered Hexagonal <i>P6mm</i>	4.9
PMO-25	1.9 ± 0.1	636	3.8	0.39	Ordered Hexagonal <i>P6mm</i>	4.7
PMO-75	1.72 ± 0.06	1052	3.5	0.75	Partly Ordered Hexagonal <i>P6mm</i>	4.5
PMO-100	1.50 ± 0.05	782	3.5	0.49	Partly Ordered Hexagonal <i>P6mm</i>	4.9

Table 1. Structural and textural parameters of the samples.

The SSA and pore volume values presented in Table 1 show a direct correlation between them. For each given sample, SSA varies practically in the same way as pore volume does. Although all samples have SSA values ranging in the 800 – 1000 m²/g range, PMO-25 exhibits a substantially decreased SSA and pore volume compared to the rest. It can be that the partial introduction of BTB over TEOS has induced local stacking faults lying in the sub-nanometer region. It is plausible to assume the existence of cavities that are inaccessible to N₂ resulting in an underestimation of the SSA when assessed by N₂ as the probe molecule. In addition, the low pore volume of PMO-25 further suggests the presence of cavities that H₂ can most likely access but are inaccessible by N₂. In the case of the pycnometry measurements He was used as the probe molecule that possesses a kinetic diameter of similar size to the one of H₂. When comparing the density value of PMO-25 although it lies between the values of PMS and PMO-75 it is still closer to the values of PMO-75 and PMO-100 than the value of PMS as one would anticipate. We believe that this low density value further suggests the presence of blocked, inaccessible cavities that make the material appear less dense than it actually is.

When we check the mesoporosity, by moving from PMS (100% TEOS) to PMO-25 (75% TEOS, 25% BTB) the latter has a considerably wider PSD. In a similar way PMO-75 exhibits wider PSD compared to PMS and PMO-100. The co-existence of 2 building units results in a structure with diverse pore sizes and consecutively diverse adsorption sites. In other words the hybrid materials possess a wider PSD and wider adsorption sites diversity close to the micro-/mesopore border regime which are of high importance for hydrogen and methane physisorption.

Scanning Electron Microscopy (SEM) provides an excellent morphological overview of the synthesized materials in the μm -scale. Figure 3 shows the SEM images of one hybrid (PMO-25) and one non-hybrid organosilica (PMO-100). The PMO-25 sample shows macroscopic hexagonal shaped crystals merged with some bulkier crystals of irregular shape and size (Fig. 3, left) of approximately 1 μm diameter (Fig. 3, middle). This indicates a long range organization of the microscopic ordering that the XRD patterns revealed. On the other hand the PMO-100 sample shows a crystal array of irregular shape and size indicating no long-range periodicity (Fig. 3, right), verifying the picture that the PXD patterns revealed for the material's order in the nanoscale (absence of (110) and (200) reflections).

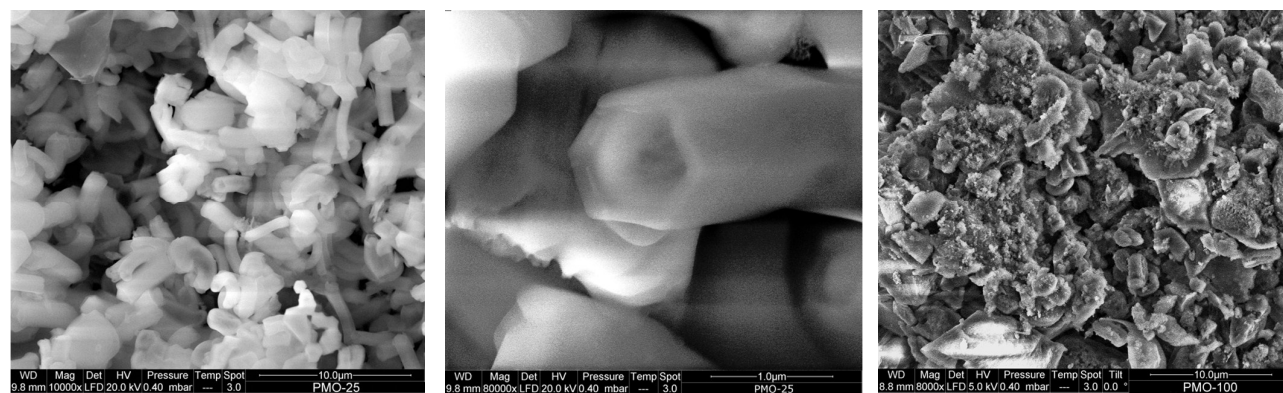


Fig 3 SEM images of PMO-25 (left) and PMO-100 (right). A higher magnification of PMO-25 is provided in the middle.

Hydrogen adsorption isotherms obtained at 77 K for all the samples are shown at Fig. 4. The amount of adsorbed hydrogen increases following a Langmuir-type curve and the desorption isotherms follow the adsorption ones. Desorption coincides fairly well in the low pressure regime however a small hysteresis is observed that could be attributed to the relatively strong adsorbent-adsorbant interaction that these materials exhibit combined with the relative small surface coverage in those conditions. In adsorption for pressures higher than 1.0 MPa the Tóth equation fitting describes the experimental data with precision higher than the Langmuir equation³⁰. Both PMO-25 and PMO-75 exhibit up to 15% higher sorption capacity than the non-hybrid materials. Additionally their sorption capacity appears enhanced in the low pressure (< 1.0 MPa) regime compared to PMS and PMO-100. The latter ones exhibit between them comparable sorption behavior in all the examined pressure range. PMO-75 is the only sample that exceeded 2.0 wt% sorption capacity in H₂ at 7.0 MPa. Its higher sorption capacity is attributed to its larger surface area compared to the other samples. This value is substantially lower than 9.0 wt% at 5.6 MPa that NU-110 has achieved and is one of the highest values reported at cryogenic conditions today³¹. It is important to note that NU-110 MOF possesses a SSA of 6143 m²g⁻¹ and 2.82 cm³g⁻¹ pore volume, values that are six and four times higher to those of PMO-75, respectively. At the same time, the SSA values of the probed Mesoporous Organosilicas samples (Table 1) are among the higher SSA values found for their class of materials³². Furthermore, excessively large pore apertures like those found in some MOFs¹⁰ can make the material more suitable for applications such as catalysis or selective inclusion of proteins and less for gas storage applications. The high pore volume means higher amount of gas stored within the material pore but not necessarily physisorbed. Once the adsorbant pore surface is farther than the optimal adsorbent-adsorbant distance, due to the Lenard-Jones potential³³ its effect on gas density compared to compressed gas³⁴ vanishes.

Measurements were repeated on the same samples kept in air for 6 months and the results are fully reproducible; these HMO

materials appear stable while aging at ambient temperature and being exposed to atmospheric moisture.

In order to get a deeper insight in the molecule – pore surface interaction, the experimentally obtained data are fitted with the Tóth model³⁰ according to the equation:

$$wt\% = wt\%_{max} \frac{K P}{(1+(K P)^t)^{\frac{1}{t}}} \quad (1)$$

where wt%_{max} is the asymptotic maximum storage capacity, K is the equilibrium constant, P the pressure and t is a parameter introduced from Tóth in order to describe the homogeneity grade of the sample surface. Tóth equation fitting parameters of the samples are summarized in Table 2.

The hydrogen and methane excess adsorption values for the samples at 77 K and 7.0 MPa for hydrogen and at 298 K and 3.5 MPa for methane are listed in Table 3.

Another important parameter to examine when studying newly developed porous adsorbents is how their performance is affected after taking into consideration fuel cells minimum pressure requirements³⁵. For the latter a higher than ambient minimum operational pressure is recommended in case it is required to vent the system to the atmosphere without a pump. DoE has issued minimum storage system delivery pressure targets of 0.5 MPa for 2020 and 0.3 MPa eventually³. Practically this means that weak low pressure interaction is desired while maintaining the material's maximum gas storage capacity. Table 3 shows the working capacity of each of the materials. Clearly the hybrid materials store higher amount of hydrogen in the 0.5-7.0 MPa region compared to the single-precursor materials.

Moving to the methane adsorption on the HMO samples at RT, adsorption (close symbols) and desorption (open symbols) isotherm curves are presented in Fig. 5. The isotherm curves shape is in agreement with the Type I IUPAC curve and the overall shape is also representative of the isotherms behaviors obtained at 286 K and 313 K on the same samples (Fig. 6, here presented only for the PMO-75 sample). The desorption isotherm curves follow the adsorption isotherms however a small hysteresis is observed as it occurred in the hydrogen adsorption measurements suggesting a strong adsorbent-

adsorbant interaction. In the end the loop closes at zero adsorption indicating that the methane adsorption is a fully reversible procedure.

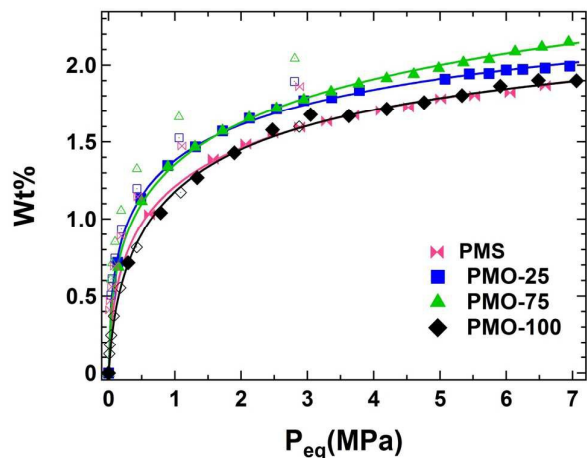


Fig 4 Hydrogen adsorption (full markers) and desorption (empty markers) isotherms obtained at 77 K and up to 7 MPa for the Hybrid Mesoporous Organosilicas samples. Lines between points represent the adsorption data fitting procedure based on the Tóth model.

Another possibility is that we observe this hysteresis due to the slow kinetics of methane adsorption/desorption processes. This could be the case when the samples show a high microporosity where diffusion could be a rate-limiting phenomenon. As we show in the PSD analysis, HMOs have mainly mesoporous structure (pore sizes are close to 3 nm). As a matter of fact, a similar behavior is observed in the hydrogen sorption analysis on the same samples suggesting that an eventual role of the structure could result in a different isotherm cycle shape.

Among all the samples, PMS had the lower methane uptake whereas the phenyl ring containing samples showed significantly enhanced sorption capacity compared to PMS. PMO-25 shows the second better performance with 2.85 wt% followed by PMO-100 with 3.5 wt% uptake. PMO-75 exhibited the highest experimental methane uptake of 4.2 wt% at 3.5 MPa. In fact, 100% substitution of TEOS with BTB results in 50% increase in material's methane sorption capacity.

The aforementioned results suggest that in methane the synergetic effect of high SSA (PMO-75) and substitution of TEOS by phenyl rings in the pore walls (PMO-75 & PMO-100) leads to increased methane sorption capacity compared to PMS and PMO-25. The enhanced interaction of methane molecule with the phenyl rings is evident in the low pressure regime that PMS has the lowest performance and consequently is reflected in the K -value of the Tóth fitting model (Table 2). Table 3 presents the gravimetric and volumetric methane excess adsorption capacities of the samples. For the calculation of the volumetric uptakes, the apparent density (0.17 g/cm^3 as calculated in our setup) of the samples was taken into account.

The evaluation of the adsorbed molecules per nm^2 ($N_{\text{molec}}/\text{nm}^2$) could indicate the efficacy of the pore surface to create more than one monolayer and can be evaluated by using the formula²⁴:

Please do not adjust margins



Journal of Materials Chemistry A

ARTICLE

	<i>H₂ Adsorption</i>				<i>CH₄ Adsorption</i>			
	PMS	PMO-25	PMO-75	PMO-100	PMS	PMO-25	PMO-75	PMO-100
wt%_{max}	3.30 ± 0.02	4.45 ± 0.05	5.05 ± 0.07	3.09 ± 0.05	3.50 ± 0.90	4.00 ± 0.40	6.40 ± 0.02	4.50 ± 0.20
K(MPa)⁻¹	11.78 ± 0.09	61.30 ± 0.50	43.40 ± 0.40	5.80 ± 0.10	0.20 ± 0.05	0.50 ± 0.07	0.25 ± 0.01	0.50 ± 0.08
t	0.36 ± 0.01	0.23 ± 0.01	0.25 ± 0.02	0.42 ± 0.03	0.70 ± 0.10	0.60 ± 0.15	0.72 ± 0.03	0.90 ± 0.02

Table 2. Tóth equation fitting parameters of the samples for Hydrogen and Methane adsorption.

Sample	Grav. H ₂ (wt.%)	H ₂ Molecules/nm ²	H ₂ Working capacity (wt%) ^c	Grav. CH ₄ (wt.%)	Vol. CH ₄ (v/v) ^a	Vol. CH ₄ (v/v) ^b	CH ₄ Molecules/nm ²	CH ₄ Working capacity (wt%) ^c
PMS	1.90	5.90	0.88	2.17	6.05	35.73	0.86	1.90
PMO-25	2.03	9.40	1.16	2.69	7.27	36.20	1.58	2.14
PMO-75	2.15	6.05	1.05	4.23	10.92	39.63	1.51	3.63
PMO-100	1.90	7.30	0.95	3.37	8.84	36.55	1.62	2.52

^a Apparent densities, skeleton densities and ideal gas law for equivalent CH₄ volume at standard temperature and pressure (STP) were used for the calculations.

^b Apparent densities, skeleton densities and ideal gas law for equivalent CH₄ volume at 298 K and 3.5 MPa were used for the calculations.

^c Defined as the difference of methane uptake between 35 bar and 5 bar.

Table 3. Gravimetric adsorption capacities, number of molecules adsorbed per nm² of the pore surface and working capacities in both hydrogen and methane for each of the samples. In the methane case, the volumetric excess adsorption capacities are reported too. All values are referred to the maximum analyzed pressure, 3.5 MPa and 7.0 MPa for methane and hydrogen, respectively.

Please do not adjust margins

Journal of Materials Chemistry A

ARTICLE

$$\frac{N_{molec}}{nm^2} = \frac{N_A \times wt\%}{10^{20} \times MW_{GAS} \times SSA} \quad (2)$$

where N_A is the Avogadro's number, wt% the gravimetric adsorption, MW_{GAS} the molecular weight of the adsorbed gas and SSA the specific surface area obtained by the BET method.

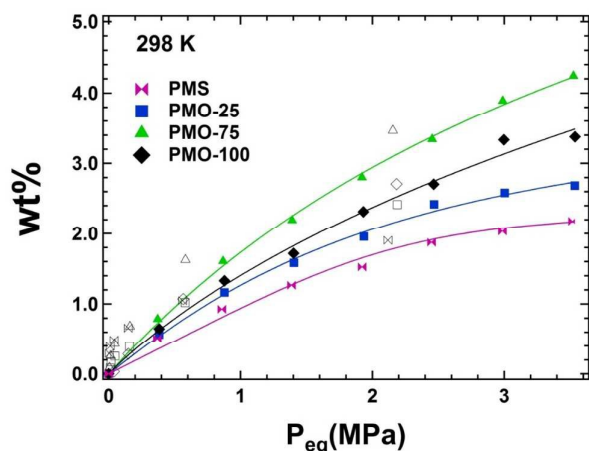


Fig 5 Methane excess adsorption (close symbols) and desorption (open symbols) isotherms obtained at 298 K and up to 3.5 MPa for all the HMO samples. Lines between points represent the data fitting based on the Tóth model.

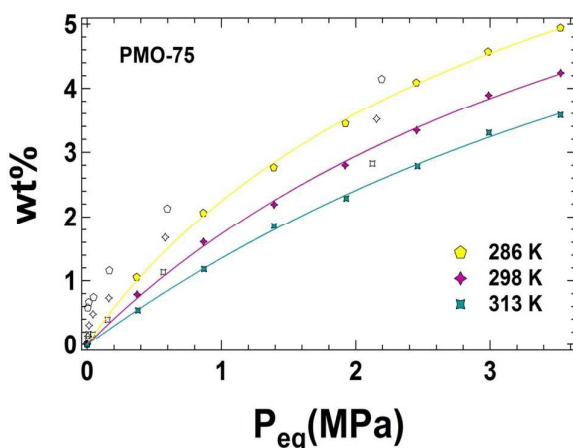


Fig 6 Methane excess adsorption and desorption isotherms obtained at 286 K (yellow), 298 K (pink) and 314 K (green) up to 3.5 MPa for the sample PMO-75 (markers). Lines between points represent the data fitting based on the Tóth model.

In the case of hydrogen, one monolayer is formed when approximately 8 H_2 molecules per nm^2 are uptaken by the surface²⁴. Fig. 7 shows the number of H_2 molecules adsorbed per nm^2 of the samples in the 0–7 MPa pressure range. At 77 K and 7.0 MPa only the PMO-25 sample forms a monolayer of adsorbed H_2 on its surface. The other samples accommodate no more than 6.0–7.3 H_2 molecules on their surface under the same conditions.

The favourable effect of microporosity on the adsorbent's sorption properties has been demonstrated by both theoretical³⁶ and experimental works³⁷. For example, Co(HBTC)(4,4'-bpy) possesses pores in the 0.5 – 0.8 nm range and relatively low SSA for a MOF framework ($887 \text{ m}^2\text{g}^{-1}$)³⁸. However the material exhibited 2.05 wt% excess adsorption capacity at 77 K and 6.5 MPa. In principle, a material possessing narrow PSD with pore size sufficient enough to accommodate a monolayer of adsorbant on its surface would be ideal in terms of adsorbent-adsorbant interaction strength. However in a real life system it is quite challenging to obtain a porous network with a narrow PSD. After the post-synthesis treatment a distribution of pores possessing different diameters is the most common result. Hence, it makes more sense to talk about the material's PSD fraction with a particular pore diameter regime over the total amount of pore sizes available.

Sample	2.0-2.5 nm	2.5-3.5 nm	3.5-4.5 nm	>4.5 nm
PMS	0%	1.5%		
PMO-25	4.6%	48.5%		
PMO-75	4.5%	54.4%		
PMO-100	0%	68.7%		

Table 4 PSD fractions of the samples, close to the micro-/mesopore border regime.

Going back to Figure 2, as we already noted, PMO-25 and PMO-75 are the only samples containing pores in the micro-/mesopore border regime (< 2.7 nm). By calculating the ratio between the area below a given PSD regime and the total area, it is interesting to correlate the sorption properties with the pore size of each material in a more direct and quantitative way. From integration of the area below each PSD Table 4 is obtained that shows the PSD fraction of each sample in the low mesopore regions of 2.0 - 2.5 nm, 2.5-3.5 nm, 3.5-4.5 nm and >4.5 nm. In fact, PMS and PMO-100 (non-hybrid PMOs) are the only samples without any pores below 2.5 nm (Fig 2). The BTB-containing samples show an increase in the percentage of pores within the 2.5-3.5 nm regime as the BTB

content increases. At the same time almost 96% of PMS's pores lie in the 3.5 – 4.5 nm range. PMO-100 possesses 68.7% of its pores within the 2.5 – 4.5 nm regime and has no pores with width below 2.5 nm or above 4.5 nm. On the other hand, both PMO-25 and PMO-75 have approximately 4.5% of their pores with diameter in the 2.0-2.5 nm regime and 17.8 and 12.6% of their pores in the 2.0-2.7 nm regime (not shown in Table 4), respectively. PMO-100 that also has relatively high fraction of pores in the 2.5-3.5 nm regime has no pores with diameter smaller than 2.7 nm. These could partially explain both hybrid materials higher K -value they exhibited in hydrogen compared to the non-hybrid PMOs. Finally, this pore size diversity indicates adsorption site heterogeneity as the low t -value of both hybrid PMOs obtained from the Tóth model fitting shows (Table 3, H_2 adsorption).

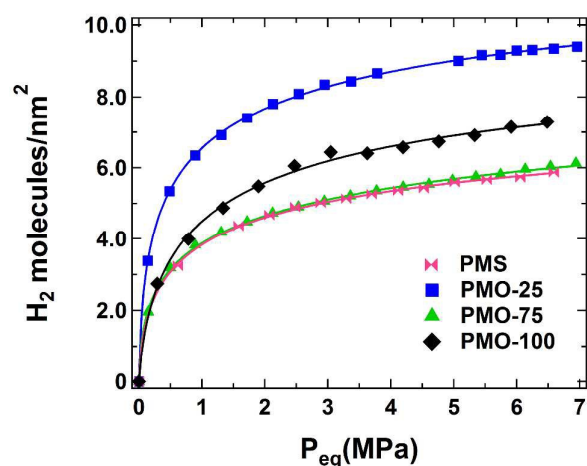


Fig 7 Number of H_2 molecules adsorbed per nm^2 versus pressure for each of the samples (markers). Lines between points represent the data fitting procedure based on the Tóth model.

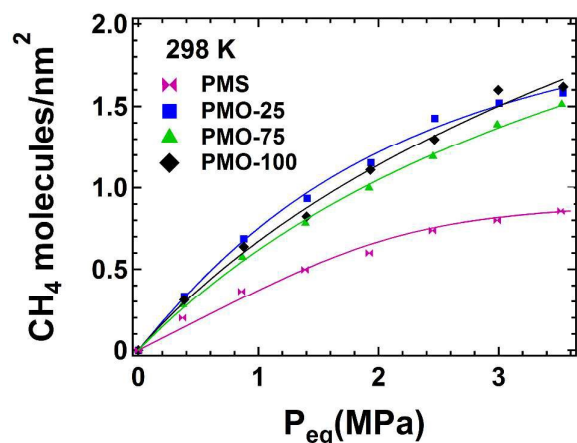


Fig 8 Number of CH_4 molecules adsorbed per surface's nm^2 versus pressure for each of the samples (markers). Lines between points represent the data fitting procedure based on the Tóth model.

Coming back to methane, the molecule's diameter is approximately 0.375 nm as different theoretical and

experimental works have calculated³⁹. Consecutively, for methane storage, the formation of one monolayer is reached when approximately 3 molecules per nm^2 are adsorbed. At the highest experimental pressure, none of the samples forms a monolayer (Fig. 8 and Table 3). On the other hand, 100% substitution of TEOS with BTB results in 100% increase in the number of methane molecules the adsorbent's surface can host (see Fig. 8). In particular, all the samples containing a certain degree of TEOS show similar values of methane adsorbed molecules whereas the PMS sample adsorbs a significantly lower number of methane molecules per nm^2 . Despite the insertion of phenyl rings having introduced local randomness on the structure of these materials (Fig 1) it does not seem to have any negative effect on the sorption properties. As it has been recently demonstrated in a spectroscopic and theoretical study, methane can interact simultaneously with faces and edges of phenyl rings. This interaction actually favors both monodentate and bidentate configurations of methane molecules around the phenyl rings⁴⁰. The XRD patterns of our materials (Fig 1) suggest that we have phenyl rings randomly arranged on the surface with either their edges or faces exposed and accessible to methane. It is interesting to note that PMO-25 although it contains just a fraction of phenyl rings compared to PMO-75 and PMO-100 it exhibits similar methane density on its surface like the BTB-based adsorbents.

A number of both theoretical and experimental studies have demonstrated that there is a variety of parameters combined together that affect the overall methane adsorption on a surface⁴¹⁻⁴³. Accessible SSA, pore volume, isosteric heat of adsorption and pore topology should be assessed collectively to understand the role of a surface on the methane adsorption. In addition to these, methane has been found to preferentially adsorb on physically tight spaces⁴⁴. Although there is a series of parameters that synergically affect the methane adsorption we believe that the random arrangement of phenyl rings on the walls could create a rough surface with physical cavities that are big enough to interact with a methane's hydrogen but not large enough to fit N_2 and affect the measured SSA. Recently, a detailed study of methane adsorption on SBA-15 carried out by small angle neutron scattering (SANS), showed that surface roughness is an important parameter that can affect the overall gas storage capacity⁴⁵. Combining this with the fact the phenyl rings can interact with CH_4 either with faces or with edges it could partially explain the increased methane density (CH_4 molecules per nm^2) that PMO-25 exhibits. A logical question that rises is why PMO-75 and PMO-100 that have higher phenyl ring concentration do not show increased methane density compared to PMO-25. Based on Fig 8, it seems that only 25 mol% of BTB is required to double the amount of methane uptake and to increase the surface coverage. Further enhancement on methane adsorption could occur once methane finds itself in a pore with diameter 3 times its kinetic diameter⁴⁴.

All samples' adsorption isotherms were fitted with the Tóth model³⁰ and the results are shown in Table 2. Similar to

hydrogen, the maximum uptake $\text{wt}\%_{\text{max}}$ is only presented as one of the three Tóth parameters but is not further analyzed as it is an extrapolated theoretical saturation capacity in very high pressures that does not fall within the examined pressure range. PMS and PMO-75 samples exhibit the lowest K -value, indicating a weak interaction between the methane molecules and the adsorbent's surface. Although PMO-75 sample's sorption capacity lies in the lower end of the TEOS containing samples, the material continues increasing its uptake until the end of the pressure scale due to its relatively large SSA (Fig. 8). Its sorption behavior suggests a diversity of adsorption sites that is reflected in its low t -value. PMO-25 has slightly higher capacity in the middle of the pressure range suggesting that its smaller pores could be the driving force enhancing the methane adsorption compared to the other samples. It appears that the absence of TEOS (PMS sample) increases the surface homogeneity and therefore the adsorption sites homogeneity as it demonstrated in Table 3 and as the PSD graph suggests in Fig. 2. Table 3 shows the working capacity of the materials in the 0.5-3.5 MPa pressure regime. Contrary to hydrogen, in methane the materials working capacity is only 13-25% less than their absolute capacity at 3.5 MPa. PMS and PMO-75 exhibit 13 and 15% capacity loss, respectively. At the same time they are the materials with the lowest K -value (0.2 and 0.25 respectively) suggesting a weaker interaction between the surface and the methane molecules.

The isosteric heat of adsorption was evaluated according to the Clausius–Clapeyron equation:

$$\ln P = -(\Delta H/RT) + C \quad (2)$$

The formula has been applied on the isotherm curves obtained on the investigated samples at 285 K, 298 K and 314 K and low pressures (0.01 MPa – 0.1 MPa). Similar values of isosteric heat of adsorption, within the error, were found for the two TEOS-based samples (PMS and PMO-25) and the two BTB-based (PMO-75 and PMO-100) samples (see Fig. 9). This suggests that in low pressures and coverages the simultaneous presence of BTB and TEOS precursors didn't play an important role in the adsorption capacity of the samples. Under those conditions the TEOS-based materials exhibited stronger interaction with the methane molecules.

Sample	ΔH (kJ/mol)	Error (kJ/mol)
PMS	15.00	± 0.50
PMO-25	14.90	± 0.40
PMO-75	12.70	± 0.70
PMO-100	12.60	± 0.80

Table 5 Calculated isosteric heat of adsorption and its error for all the samples. The values have been obtained for low pressures and coverages.

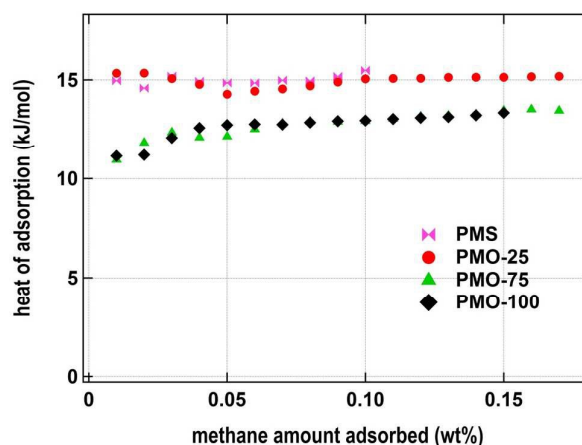


Fig 9 Isosteric heat of adsorption versus methane amount adsorbed.

The isosteric heat of adsorption is directly connected with the interaction between adsorbed molecules and surface⁴⁶. When this interaction is attractive the heat of adsorption increases with the increase of the loading. When on the other hand the heat of adsorption decreases with the increase of the loading, then either there is repulsion between the adsorbant and the surface or we have a heterogeneous surface. In general, the adsorbant molecules prefer to be adsorbed by higher energy adsorption sites and then, as the pressure gradually increases, to be adsorbed by lower energy adsorption sites. Thus, a decrease in the value of isosteric heat of adsorption is anticipated. If though its value remains stable despite the increase in the loading then we have an energetically homogeneous surface⁴⁶.

If we have a closer look at Fig 9, in the 0 – 0.05 wt% regime, PMO-75 and PMO-100 exhibit a relevantly steep enthalpy increase which practically remains the same with only a minor positive slope to be observed in the 0.05 – 0.18 regime. On the other hand samples PMS and PMO-25 show a decrease in the enthalpy value in the first coverage region (0 – 0.05 wt%). Then a small increase in the 0.05 – 0.10 wt% regime follows and above that coverage it remains stable until the end of the investigated scale. Practically there is an increase in the enthalpy value for samples PMO-75 and PMO-100, with PMO-75 showing a 2-step increase, whereas there is a decrease for PMS and PMO-25 that afterwards restores its initial value (~ 15 kJ/mol).

Now, the t -value of PMO-100 in methane (Table 2) is high suggesting a surface with high degree of homogeneity, whereas the other samples have a lower t -value suggesting they have more heterogeneous surfaces. At the same time, the K -value from Tóth also provides information on the binding energy between adsorbate and surface. However, it is important to point out that, the Tóth parameters are used to describe the isotherm macroscopically whereas the isosteric heat of adsorption evaluation applied here focuses specifically on the 0-1 bar regime and it is a tool to help us get an insight on the interplay between adsorbant and adsorbent in those

low coverage conditions. To sum up, the shape of the graphs in the 0-0.05 wt% regime suggests a competition between attractive and repulsive interaction with the repulsive effect being stronger in the BTB-based samples under those temperature, pressure and surface coverage conditions.

Our materials have lower values of isosteric heat of adsorption compared to PCN-14 (18.7 kJ/mol)⁴⁷ or UTSA-20 (18.2 kJ/mol)⁴⁷ that exhibit some of the highest reported values up to day. However, PMS and PMO-25 have similar isosteric heat of adsorption as NU-125 (15.1 kJ/mol)⁴⁸ and other high performing CH₄ sorbents such as UTSA-76⁴⁹, NOTT-101 and UTSA-80a⁵⁰ that have values in the 15-16 kJ/mol regime. NU-111⁴⁸, an adsorbent with particular high SSA (4930 m²g⁻¹) lies at the 14 kJ/mol regime.

Conclusions

In this study, PMOs having BTB, TEOS or a mixture of them (hybrid PMOs) as precursors were synthesized and characterized by means of XRD, BET, IR, SEM and He pycnometry. Their hydrogen and methane sorption capacity, kinetics and reversibility were investigated with a Sieverts apparatus. XRD, IR and He pycnometry verified the successful incorporation of the phenyl rings into the material. The increased amount of BTB in the starting ratio was correlated with a decrease in the material density and increase in its degree of amorphousness. The sample with 75% substitution of TEOS by BTB (PMO-75) was found to possess the highest SSA compared to the other samples. The hybrid materials demonstrated enhanced sorption properties in hydrogen in pressures up to 7.0 MPa and at 77 K. The highest hydrogen storage capacity was found when TEOS was exchanged by 25 mol% with BTB. The examined materials exhibited excellent reversibility over multiple adsorption-desorption cycles. In methane, the synergetic effect of high SSA with substitution of TEOS by phenyl rings in the pore walls led to increased methane sorption capacity. All the phenyl ring-containing samples exhibited enhanced sorption capacity with the hybrid PMO-75 sample having the highest adsorption capacity compared to the other samples. The combined use of precursors led to materials with wider PSD and higher fraction of pores close to the micro-/mesopore border regime compared to the single-precursor materials, allowing the formation of smaller pore sizes that consequently favor the adsorption interaction. Quantitative correlation of the PSD with the materials sorption behavior verified that careful tailoring of the material's PSD is required to increase the adsorbent-adsorbant interaction. The Tóth fitting model suggested that all the TEOS containing samples showed similar but not high degree of surface homogeneity. For low pressures and surface coverages, similar values of isosteric heat of adsorption were found, within the error, for the two TEOS-based samples (PMS and PMO-25) and the two BTB-based (PMO-75 and PMO-100) samples. The results of this study suggest that research should focus in optimizing the synthesis of porous networks aiming in increased SSA bearing in mind that tailored pore size and suitable selection of building units

need to be strongly taken into consideration depending on the diameter of the adsorbant fluid and the polarity degree of its bonds.

Acknowledgements

Innova S.r.l. is gratefully acknowledged for financial support. The authors want to deeply thank Giovanni Desiderio from CNR-IPCF LiCryL for obtaining the SEM images. A.E. gratefully acknowledges the Academy of Athens, Greece for a PhD fellowship. G.N.K and M.K.A. are thankful to the International Doctoral School of Science and Technology "Bernardino Telesio" of the University of Calabria, Italy for their ph.D fellowship. This work was partially supported by the EOMAT PON03PE_00092_1 project.

*Correspondence - gkalant@gmail.com

References

- G. W. Crabtree, M. S. Dresselhaus and M. V. Buchanan, *Phys. Today*, 2004, **57**, 39-44.
- A. Züttel, A. Borgshulte and L. Shlapbach, *Hydrogen as a Future Energy Carrier*, Wiley-VCH Verlag GmbH & Co. KGaA, Weinheim, 1st edn., 2008.
- U.S. Department of Energy. Technical System Targets: Onboard Hydrogen Storage for Light-Duty Fuel Cell Vehicles., http://energy.gov/sites/prod/files/2015/01/f19/fcto_myrd_table_onboard_h2_storage_systems_doe_targets_ldv.pdf, 2012).
- Fuel Cells and Hydrogen Joint Undertaking, <http://www.fch-iu.eu/>, <http://www.fch-iu.eu/>.
- A. Züttel, *Naturwissenschaften*, 2004, **91**, 157-172.
- B. Sakintuna, F. Lamari-Darkrim and M. Hirscher, *Int. J. Hydrog. Energy*, 2007, **32**, 1121-1140.
- T. D. Humphries, G. N. Kalantzopoulos, I. Llamas-Jansa, J. E. Olsen and B. C. Hauback, *J. Phys. Chem. C*, 2013, **117**, 6060-6065.
- G. N. Kalantzopoulos, M. N. Guzik, S. Deledda, R. H. Heyn, J. Muller and B. C. Hauback, *Physical Chemistry Chemical Physics*, 2014, **16**, 20483-20491.
- G. Liang, S. Boily, J. Huot, A. Van Neste and R. Schulz, *J. Alloy. Compd.*, 1998, **268**, 302-307.
- H. Furukawa, K. E. Cordova, M. O'Keeffe and O. M. Yaghi, *Science*, 2013, **341**, 974-+.
- J. Shen, J. Sulkowski, M. Beckner and A. Dailly, *Microporous and Mesoporous Materials*, 2015, **212**, 80-90.
- G. N. Kalantzopoulos, E. Maccallini, A. Policicchio, I. Krkljus, F. Ciuchi, G. Golemme, M. G. Buonomenna, M. Hirscher and R. G. Agostino, *Microporous and Mesoporous Materials*, 2015, DOI: 10.1016/j.micromeso.2015.08.039.
- K. L. Lim, H. Kazemian, Z. Yaakob and W. R. W. Daud, *Chemical Engineering & Technology*, 2010, **33**, 213-226.
- D. J. Tranchemontagne, K. S. Park, H. Furukawa, J. Eckert, C. B. Knobler and O. M. Yaghi, *J. Phys. Chem. C*, 2012, **116**, 13143-13151.

15. S. S. Han and W. A. Goddard, *Journal of the American Chemical Society*, 2007, **129**, 8422-+.
16. A. Mavrandonakis, E. Tyliaakis, A. K. Stubos and G. E. Froudakis, *J. Phys. Chem. C*, 2008, **112**, 7290-7294.
17. O. M. Yaghi, M. O'Keeffe, N. W. Ockwig, H. K. Chae, M. Eddaoudi and J. Kim, *Nature*, 2003, **423**, 705-714.
18. F. Svec, J. Germain and J. M. J. Frechet, *Small*, 2009, **5**, 1098-1111.
19. A. Mavrandonakis, E. Klontzas, E. Tyliaakis and G. E. Froudakis, *Journal of the American Chemical Society*, 2009, **131**, 13410-13414.
20. B. J. Melde, B. T. Holland, C. F. Blanford and A. Stein, *Chem. Mat.*, 1999, **11**, 3302-3308.
21. S. Inagaki, S. Guan, T. Ohsuna and O. Terasaki, *Nature*, 2002, **416**, 304-307.
22. W. J. Hunkes and G. A. Ozin, *Chem. Mat.*, 2004, **16**, 5465-5472.
23. F. Hoffmann, M. Cornelius, J. Morell and M. Froba, *Angewandte Chemie-International Edition*, 2006, **45**, 3216-3251.
24. G. N. Kalantzopoulos, A. Enotiadis, E. Maccallini, M. Antoniou, K. Dimos, A. Policicchio, E. Klontzas, E. Tyliaakis, V. Binas, P. N. Trikalitis, R. G. Agostino, D. Gournis and G. E. Froudakis, *Int. J. Hydrog. Energy*, 2014, **39**, 2104-2114.
25. K. Dimos, M. K. Antoniou, A. Meichanetzoglou, S. Lymperopoulou, M. D. Ouzouni, I. B. Koutselas, D. Fokas, M. A. Karakassides, R. G. Agostino and D. Gournis, *Microporous and Mesoporous Materials*, 2012, **158**, 324-331.
26. M. K. Antoniou, A. Policicchio, K. Dimos, D. Gournis, M. A. Karakassides and R. G. Agostino, *Microporous and Mesoporous Materials*, 2012, **158**, 332-338.
27. M. Thommes, K. Kaneko, A. V. Neimark, J. P. Olivier, F. Rodriguez-Reinoso, J. Rouquerol and K. S. W. Sing, *Pure and Applied Chemistry*, July 2015, **87**, 1051-1069.
28. J. Rouquerol, P. Llewellyn and F. Rouquerol, *Studies in Surface Science and Catalysis*, 2007, **160**, 49-56.
29. A. Policicchio, E. Maccallini, G. N. Kalantzopoulos, U. Cataldi, S. Abate, G. Desiderio and R. G. Agostino, *Review of Scientific Instruments*, 2013, **84**.
30. J. Toth, *Acta Chimica Academiae Scientiarum Hungaricae*, 1962, **32**, 39-&.
31. O. K. Farha, A. O. Yazaydin, I. Eryazici, C. D. Malliakas, B. G. Hauser, M. G. Kanatzidis, S. T. Nguyen, R. Q. Snurr and J. T. Hupp, *Nature Chemistry*, 2010, **2**, 944-948.
32. P. Van der Voort, D. Esquivel, E. De Canck, F. Goethals, I. Van Driessche and F. J. Romero-Salguero, *Chemical Society Reviews*, 2013, **42**, 3913-3955.
33. B. H. Panella, Michael, in *Handbook of Hydrogen Storage*, ed. M. Hirscher, Wiley-VCH Verlag GmbH & Co. KGaA, Weinheim, Germany, 2010, DOI: 10.1002/9783527629800.ch2.
34. F. D. Minuto, A. Policicchio, A. Aloise and R. G. Agostino, *Int. J. Hydrog. Energy*, DOI: <http://dx.doi.org/10.1016/j.ijhydene.2015.07.029>.
35. N. P. Stadie, J. J. Vajo, R. W. Cumberland, A. A. Wilson, C. C. Ahn and B. Fultz, *Langmuir*, 2012, **28**, 10057-10063.
36. S. K. Bhatia and A. L. Myers, *Langmuir*, 2006, **22**, 1688-1700.
37. M. P. Suh, H. J. Park, T. K. Prasad and D. W. Lim, *Chemical Reviews*, 2012, **112**, 782-835.
38. Y. Li, L. Xie, Y. Liu, R. Yang and X. Li, *Inorganic Chemistry*, 2008, **47**, 10372-10377.
39. K. Mosher, Master of Science Thesis, Stanford University, 2011.
40. M. Errahali, G. Gatti, L. Tei, L. Canti, A. Fraccarollo, M. Cossi and L. Marchese, *The Journal of Physical Chemistry C*, 2014, **118**, 10053-10060.
41. T. Düren, L. Sarkisov, O. M. Yaghi and R. Q. Snurr, *Langmuir*, 2004, **20**, 2683-2689.
42. Q. Ye, S. Yan, D. Liu, Q. Yang and C. Zhong, *Molecular Simulation*, 2010, **36**, 682-692.
43. S. Wang, *Energy & Fuels*, 2007, **21**, 953-956.
44. T. A. Makal, J.-R. Li, W. Lu and H.-C. Zhou, *Chemical Society Reviews*, 2012, **41**, 7761-7779.
45. W.-S. Chiang, E. Fratini, P. Baglioni, D. Georgi, J.-H. Chen and Y. Liu, *The Journal of Physical Chemistry C*, 2016, **120**, 4354-4363.
46. D. D. Do, in *Adsorption Analysis: Equilibria and Kinetics*, Imperial College Press, 1998, DOI: doi:10.1142/9781860943829_0002.
47. R. Babarao, S. Dai and D.-e. Jiang, *Langmuir*, 2011, **27**, 3451-3460.
48. Y. Sun, T. Ben, L. Wang, S. Qiu and H. Sun, *Journal of Physical Chemistry Letters*, 2010, **1**, 2753-2756.
49. A. Ahmed, A. W. Thornton, K. Konstas, S. K. Kannam, R. Babarao, B. D. Todd, A. J. Hill and M. R. Hill, *Langmuir*, 2013, **29**, 15689-15697.
50. H.-M. Wen, B. Li, D. Yuan, H. Wang, T. Yildirim, W. Zhou and B. Chen, *Journal of Materials Chemistry A*, 2014, **2**, 11516-11522.

Enhanced Hydrogen and Methane Storage of Hybrid Mesoporous Organosilicas

Georgios N. Kalantzopoulos^a, Myrsini K. Antoniou^a, Apostolos Enotiadis^b,
Konstantinos Dimos^b, Enrico Maccallini^a, Alfonso Policicchio^a, Elio Colavita^a and
Raffaele G. Agostino^a

^aCNISM-Department of Physics, Univ. of Calabria, *via P. Bucci 33C, 87036, Rende (CS), Italy*

^bDepartment of Materials Science & Engineering, University of Ioannina, *45100 Ioannina, Greece*

For Table of Contents Only

